REVIEW

High-Pressure THz ESR

Takahiro Sakurai[1] · Hitoshi Ohta[2] · Shigeo Hara[1] · Yu Saito[1]

Abstract

In solid-state physics, pressure is an essential parameter, which can continuously change the interaction between electrons. The combination of terahertz electron spin resonance (THz ESR) with pressure is a powerful approach to clarify the spin state under pressure from the microscopic point of view, especially for quantum magnets. The most important feature of our high-pressure THz ESR system is that our pressure cell ensures the high pressure and wide frequency range using ceramics in internal parts, which are well balanced in terms of toughness and transmittance of electromagnetic waves. This approach allowed to very accurately describe the spin state under pressure. In this review, high-pressure ESR systems are reviewed with a focus on those in the high-frequency region. In addition, we show differences between other systems and our system. Moreover, we show the usefulness of our system by showing application examples of several magnetic materials of interest.

1 Introduction

In solid-state physics, extreme conditions are indispensable for the search of novel quantum phenomena. Among them, pressure P is the only parameter that can continuously change the interaction between electrons while maintaining lattice symmetry, provided that no structural phase transition occurs. However, in reality, the accurate evaluation of interaction parameters under pressure is difficult, and it often causes difficulty to approach the heart of the matter. In this paper, we show that our high-pressure terahertz electron spin resonance (THz ESR) is extremely effective in this respect.

Pressure is not the major experimental parameter in ESR measurements compared with nuclear magnetic resonance (NMR) measurement where pressure is frequently used [1]. This is the case because NMR has a resonance frequency of tens to hundreds MHz, and it is relatively easy to apply an oscillating magnetic field to

✉ Takahiro Sakurai
   tskaurai@kobe-u.ac.jp

1   Research Facility Center for Science and Technology, Kobe University, Kobe 657-8501, Japan

2   Molecular Photoscience Research Center, Kobe University, Kobe 657-8051, Japan

the sample by a coil introduced into the pressure cell. The same technique cannot be applied to ESR owing to its much higher resonance frequency [2]. Most of the previously reported high-pressure ESR techniques have focused on the combination of pressure device and resonator to provide an oscillating field to the sample under pressure [3–5].

Meanwhile, our group has performed THz ESR measurements using a pulsed high magnetic field by a simple transmission method without a resonator [6]. Specifically, a sample is placed at the center of the magnetic field, and the transmitted intensity is detected. Using this transmission-type ESR technique, we tried to perform an ESR measurement under pressure with a novel pressure cell whose internal parts, which are usually made of metal, were replaced with transparent sapphire [7]. This surprisingly simple method was highly effective and useful. This is the beginning of our high-pressure THz ESR measurement. In this paper, first, we review the history of the high-pressure ESR technique, by focusing on studies performed in the high-frequency region, and show differences from our approach. In addition, we show that our high-pressure THz ESR is very effective for the accurate evaluation of interaction parameters under pressure by providing application examples.

2 History of High-Pressure ESR

Figure 1 shows a brief summary of the history of high-pressure ESR. The first example of high-pressure ESR dates to Walsh's pioneering work in 1957 [8]. It has only been about 10 years since Zavoisky succeeded in observing electron paramagnetic resonance (EPR). A coaxial resonator was set in the pressure cell, and EPR measurement was performed at room temperature in the X-band up to 1 GPa. Since
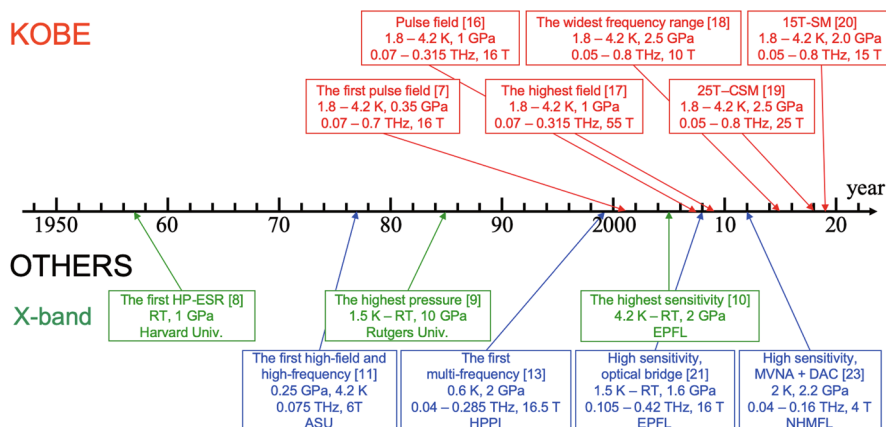

Fig. 1 History of high-pressure ESR. The upper row is our contribution; the lower row is the contribution by other groups. In the lower row, the line labeled "X-band" shows representative high-pressure X-band ESR systems. ASU and HPPI indicate Academy of Sciences of the Ukraine SSR (present-day National Academy of Sciences of Ukraine) and Institute for High Pressure Physics, respectively. See text for details (color online)

then, the high-pressure ESR system has progressed in various ways mainly in the X-band. The development has been focused on approaches to combine a resonator and a pressure device to achieve both sensitivity and high pressure. In a system, which uses a diamond anvil cell (DAC) whose gasket also works as a resonator, the pressure reached 10 GPa [9]; in a system that uses DAC and two high dielectric materials, the sensitivity reached 1/3 of that of commercially available system [10]. See other reviews for the details of these resonator-type low-frequency high-pressure ESR systems [3–5].

The first high-pressure ESR measurement using high magnetic field and high frequency has been performed by Lukin et al. [11]. A sample, whose size was adjusted to act as a type of dielectric resonator, was placed in the pressure cell to couple with microwaves. ESR measurements were performed at 75 GHz up to 0.25 GPa with the maximum field of 6 T. They used a superconducting magnet for the first time for high-pressure ESR measurements and observed the antiferromagnetic resonance (AFMR). Of note, they also used the clamp-type piston–cylinder pressure cell for the first time in a series of their studies [12]. Before their studies, methods using such as so-called bomb-type pressure cell, where an external pressure generator connected directly to the pressure cell maintains the pressure during experiment, were mainly used.

High-pressure ESR measurements using multi-frequency electromagnetic waves have been performed by Kornilov et al. [13] and by us [7]. Both studies used clamp-type pressure cells whose internal parts were made of sapphire.

It appears that Kornilov et al. began the development of the pressure cell itself before 1999 [14]. They thought that they could observe the transmitted intensity of the sample using sapphire as internal parts of the pressure cell or the reflected intensity by placing a metal foil on one side. The pressure cell consisted of two layers. An outer layer was a Ti alloy, and the inner layer was NiCrAl (outer diameter 18 mm, inner diameter 3.7 mm); the maximum pressure was reported to be 3 GPa. This pressure cell was combined with a millimeter-wave network analyzer, which was commercially available since the 1990s [15]; they observed the cyclotron resonance in the frequency range from 0.042 to 0.275 THz [13]. The temperature was 0.6 K, and the maximum magnetic field was 17 T. However, there was no follow-up report; perhaps, there was a problem with pressure generation for the reasons described later.

Our first pressure cell was made of a CuBe alloy with an outer diameter of 6 mm and an inner diameter of 3 mm to fit the bore of the pulse magnet of our high-field ESR system [7]. We succeeded in performing a world's first high-pressure ESR measurement using a pulsed high magnetic field [7]. The frequency range was 0.06 to 0.7 THz; the maximum magnetic field was 16 T; the temperature was 1.8–4.2 K. However, actually, sapphire easily broke and was not very practical. The maximum pressure, which could be repeatedly generated, was only 0.35 GPa. There was a problem with the efficiency of pressure generation owing to the poor mechanical strength of sapphire; this may be the reason why there was no follow-up report by Kornilov et al. However, the internal parts of the pressure cell do not necessarily have to be transparent, and it is sufficient that they have reasonable transmittance to the required electromagnetic wave region. Therefore, we started to use ZrO_2-based ceramics. The toughness and transmittance of ZrO_2-based

ceramics will be described later. We also used a NiCrAl alloy as the cylinder, which had a higher electric resistance, to suppress the eddy current on the pressure cell, which produced heating [16]. Finally, we achieved the maximum pressure of 1 GPa [16] and the maximum pulse field of 55 T [17] using the NiCrAl cylinder with the outer diameter of 8 mm and the inner diameter of 3 mm.

In transmission-type ESR measurements, the amount of sample directly affects the signal-to-noise ratio. In the aforementioned system, the inner diameter of 3 mm was not sufficient for the needed amount of sample, and the sensitivity remained insufficient. However, if the inner diameter is increased, the thickness of the cylinder becomes thin, and its mechanical strength decreases. Therefore, we decided to use a superconducting magnet with a large bore to improve both the sensitivity and pressure region even at the expense of magnetic field. This approach allowed us to use a large pressure cell, and we were able to develop a pressure cell with an outer diameter of 28 mm and an inner diameter of 5 mm, which consisted of a CuBe outer sleeve and a NiCrAl inner cylinder [18]. ZrO_2 -based ceramics were used for all internal parts. The maximum attainable pressure was 2.5 GPa. We developed systems that combined this pressure cell with a cryogen-free superconducting magnet with a maximum magnetic field of 10 T (abbreviated as 10T-CSM later) [18] and a cryogen-free superconducting magnet with a maximum magnetic field of 25 T (25T-CSM) [19]. In addition, we developed a system, where a slightly smaller pressure cell and a 15 T superconducting magnet (15T-SM) were combined [20]. The details of these systems will be described later.

Except for our systems, there are two major systems in the world for high-pressure ESR measurements in high magnetic field and high-frequency regions. The first system has been developed by Náfrádi et al. at the Swiss Federal Institute of Technology in Lausanne (EPFL) [21]. Using the rotation of the plane of polarization of electromagnetic wave at the resonance, the intensity can be sensitively detected through a quasi-optical bridge [22]. In addition, a corrugated tube optimized for 0.21 THz is used in the cryostat to minimize the loss of electromagnetic wave propagation. The frequency range is 0.105–0.42 THz, the maximum magnetic field is 16 T, and the temperature range is 1.5–300 K. The pressure cell is a piston–cylinder type with a Poulter-type diamond window. It is made of CuBe with the outer diameter of 25 mm and the inner diameter of 5 mm, and the maximum pressure is 1.6 GPa. Electromagnetic waves are reflected at the bottom of the sample space, and the reflected intensity is observed using the aforementioned approach. Furthermore, because the magnetic field modulation method is not suitable for the pressure cell owing to the generation of eddy currents, frequency modulation can be used.

The other system consists of a resonator and a vector network analyzer developed by Hill et al. at the National High Magnetic Field Laboratory (NHMFL) [23, 24]. The system uses a small plastic DAC that can be set in the resonator. However, the use of the plastic cell significantly increases the microwave losses in the resonator and it makes the measurements considerably more challenging than those at ambient pressure [25]. Low temperature allows to minimize losses, and the temperature range is limited below 10 K. The maximum pressure is reported to be 3.5 GPa [23]; however, the practical upper limit is approximately 2 GPa [24, 25]. The frequency

range is 0.04–0.32 THz. The angle-dependent ESR measurement under pressure is possible by combining with a vector magnet.

These systems focus on sensitivity compared with our system. Considering that they applied their systems to metal complexes [24] and organic compounds [25, 26], the high sensitivity is probably required because these single crystals are small. However, the use of a corrugated tube or resonant cavity limits available frequencies in exchange for the improvement in sensitivity. However, our high-pressure ESR system has the feature of wide frequency range up to 0.8 THz, though the sensitivity is slightly lower than that of these systems. This broadband feature is essential for understanding quantum magnets because many of them have low-lying excited states in the sub-THz region, which characterize their magnetism, as is described in Sect. 4.

3 Outline of Our High-Pressure THz ESR System

The most characteristic feature of our pressure cell is that all internal parts are made of ceramics. Figure 2a shows the frequency dependence of transmittance of several commercially available ceramics [27, 28]. It also shows K_{1c} values, which indicate the fracture toughness of these ceramics. For example, Al_2O_3 ceramic has the highest transmittance among the investigated ceramics; however, its K_{1c} value is the lowest; thus, Al_2O_3 ceramic can crack easily similar to as sapphire single crystal. Meanwhile, a 95:5 mixture of ZrO_2 and MgO has the highest K_{1c} value whereas it has the lowest transmittance. Thus, the transmittance and toughness strongly depends
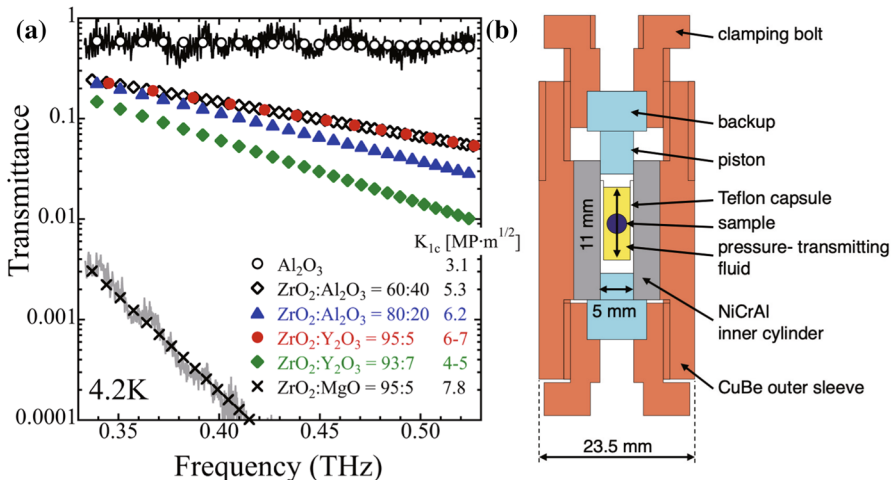

Fig. 2 a Frequency dependence of the transmittance of various ceramics. The K_{1c} value, which indicates fracture toughness, is also shown. The transmittance was measured at 4.2 K for a test piece with the same shape (12 mm ×30 mm). Because obtained data can be fitted almost linearly in a semi-logarithmic plot, only fitting results are shown except for the highest and lowest results. **b** Cross section of a hybrid-type pressure cell (color online)

on constituent. In addition, all ceramics have a decreasing tendency of transmission as a function of frequency except for Al_2O_3 ceramic. We use an 80:20 mixture of ZrO_2 and Al_2O_3 (FCY20A, Fuji Die Co., Ltd.) mainly from the viewpoint of the balance of transmittance, toughness, magnetic impurities, availability, and price. The Al_2O_3 ceramic (FCA10) is also used for the piston, which does not directly touch the pushing rod, to achieve the desired transmittance. Then the pressure and frequency ranges are optimized. The maximum pressure reaches 2.5 GPa, and a very wide frequency region from 0.05 to 0.8 THz is obtained. The lower limit of frequency is slightly lower than the cutoff frequency (0.06 THz) of the cylinder inner diameter (5 mm), because ceramics act as a dielectric and effectively reduce the cutoff frequency. The upper limit is determined by the transmittance of ceramics, output power of the light source, and available frequency range of the detector.

The cylinder of our clamp-type pressure cell is a so-called hybrid type, with the NiCrAl inner cylinder and CuBe outer sleeve; the outer and inner diameters are 28 mm and 5 mm, respectively. Although the maximum pressure is slightly reduced (2.0 GPa), we also use the smaller outer diameter (23.5 mm) with the same inner diameter (Fig.2b) [20]. In both cases, the sample space inside the Teflon capsule before applying the load is 4 mm ×11 mm. Daphne 7373 or 7474 is used as the pressure-transmitting medium. The pressure is evaluated using the relationship between the load at room temperature and the pressure at low temperature determined from the superconducting transition temperature of tin [18].

Figure 3a and (b) shows the schematic diagrams of our high-field high-pressure ESR systems using 10T-CSM [18] and 25T-CSM [19], respectively. The 25T-CSM system, which was developed at the Institute for Materials Research, Tohoku University, can generate the world's highest magnetic field among the cryogen-free superconducting magnets [29]. The high T_c superconductor is used as the inner coil, and the magnetic field of 24.6 T can be generated in a room temperature bore of 52 mm. This system has been open for joint research as a multiuse magnet since 2017. In both 10T-CSM and 25T-CSM systems, Gunn oscillators and backward traveling oscillators are used as light sources, and the transmitted electromagnetic wave through a pressure cell is detected by an InSb detector. The electromagnetic wave is rectangularly modulated electrically or mechanically, and the modulation frequency is used as a reference for the lock-in detection. In the 10T-CSM system, a bulk homemade InSb detector is positioned at the bottom of the cryostat, which has a space below the center of the magnetic field. In the 25T-CSM system, mirrors are placed at the bottom of the cryostat to draw electromagnetic waves to the outside of the cryostat, and a commercially available InSb detector with a cryostat is used. The total length of the light pipe is more than twice as long as that of the 10T-CSM system; however, the loss during the propagation of electromagnetic waves is canceled using a highly sensitive commercial InSb detector. Both systems have the temperature range of 1.8–4.2 K.

In addition to these systems, we also developed a system combined with 15T-SM, which used a reflection approach that was similar to that of the 25T-CSM system [20]. The pressure cell has a slightly smaller outer diameter (23.5 mm) as shown in Fig. 2b; thus, it can be inserted into a variable temperature insert. In principle, the temperature-dependent measurement up to 200 K is possible.
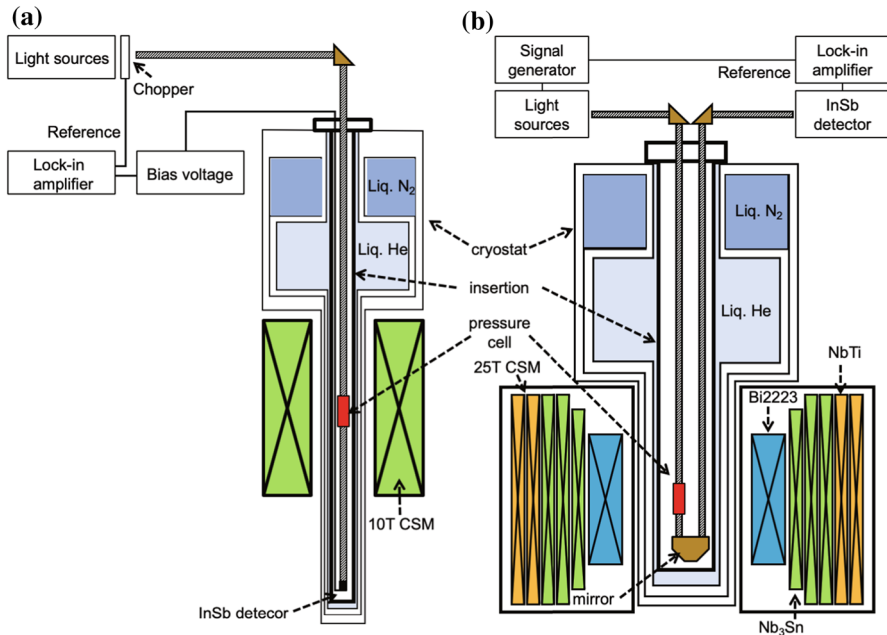
Fig. 3 Schematic diagram of high-pressure ESR systems using 10T-CSM (**a**) and 25T-CSM (**b**) (color online)

4 Application Examples of High-Pressure THz ESR

4.1 Orthogonal-Dimer Spin System SrCu$_2$(BO$_3$)$_2$ [30]

This is an application example of the 10T-CSM high-pressure ESR system. SrCu$_2$ (BO$_3$)$_2$ is well known as the orthogonal-dimer spin system [31]. The magnetic ion Cu^{2+} ($S = 1/2$) forms a dimer, and the dimers are arranged orthogonally to each other in the *ab* plane (Fig. 4a, "dimer"). If the antiferromagnetic exchange interactions of the intradimer and interdimer are J (solid line) and J' (dotted line), respectively, in the limit $J' = 0$ ($\alpha = J'/J = 0$), the system is apparently in the dimer singlet state, whereas in the opposite limit $J = 0$ ($\alpha = \infty$), the system is equivalent to a square lattice and is in the Néel state. However, in the region where J and J' compete, frustration occurs between spins, and the ground state is not trivial. Theoretically, it is expected that a peculiar quantum state called, a plaquette singlet state, which forms a singlet with four spins would appear (Fig. 4a, "plaquette") [32, 33]. However, it is still an open question whether the singlet is formed by four spins on a square including the diagonal bond J ("full type") or four spins on a square not including the diagonal bond J ("void type") [34]. SrCu$_2$(BO$_3$)$_2$ is in the dimer singlet phase at ambient pressure, and many attempts have been made to realize the plaquette singlet by applying pressure [17, 35–38]. However, because this phase transition is a non-magnetic–non-magnetic transition, it is difficult to observe it by macroscopic physical measurements such as the magnetization measurement under
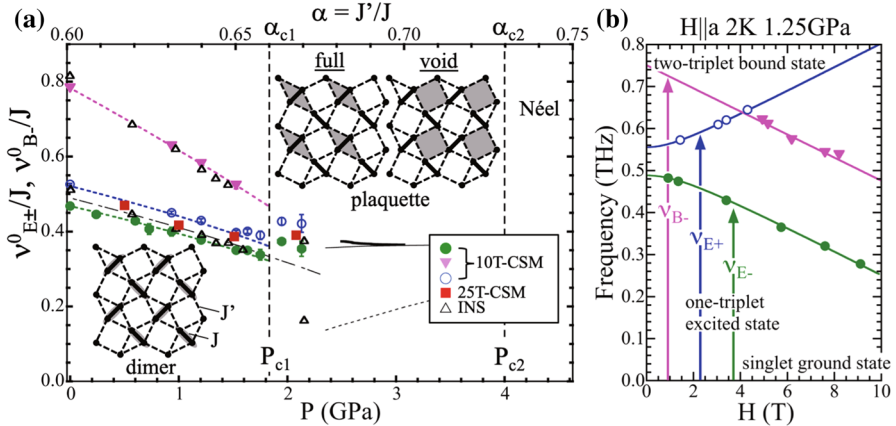
Fig. 4 **a** Pressure and interaction ratio $\alpha = J'/J$ dependence of the excitation energy normalized J obtained by the 10T-CSM system for $SrCu_2(BO_3)_2$, made by modifying Fig. 3b in Ref. [30]. The excitation energies obtained by the 25T-CSM system [19] and INS [35] are also plotted. Illustrations indicated by "dimer" and "plaquette" represent the singlet state formed by the spins in the shaded area. For the plaquette singlet state, there is a "full type", which includes the diagonal interaction J, and a "void type", which does not. **b** Frequency-field diagram for $H \parallel a$ obtained at 2 K and 1.25 GPa, made by modifying Fig. 1b in Ref. [30]. The solid curves for $\nu_{E\pm}$ are the fitting result by theoretical curves [39]. The solid line for ν_{B-} is the linear fitting result (color online)

pressure. Moreover, it was difficult to directly compare experimental results with theoretical results because the relationship between the experimental parameter P and the theoretical variable α was not clear.

We tried the high-pressure THz ESR for this system [30]. The ESR measurement can directly observe the low-lying excited states of this system [40, 41]. Figure 4b shows a typical frequency-field diagram under pressure. We observed the transition $\nu_{E\pm}$ from the singlet ground state to the $S_z = \pm 1$ states of the triplet states $S = 1$ (one-triplet excited state). In addition, the transition ν_{B-} from the ground state to the $S_z = -1$ state of the quintet states $S = 2$ (two-triplet bound state) was also observed. These excitation energies at zero magnetic field $\nu^0_{E\pm}$ and ν^0_{B-} showed monotonous decreases with pressure and the tendency was steeper at ν^0_{B-}. Furthermore, we found that $\nu^0_{E\pm}$ showed a discontinuous jump between 1.75 GPa and 1.95 GPa and the transition pressure was determined to be $P_{c1} = 1.85 \pm 0.05$ GPa.

We considered that the tendency of the excitation energy below P_{c1} can be used for the analysis, and we performed a theoretical calculation of excitation energies with α as a variable for the orthogonal-dimer lattice. Thus, the ratio $\nu^0_{E\pm}/\nu^0_{B-}$ was found to have a monotonous function for α. This means that one α corresponds to only one ratio $\nu^0_{E\pm}/\nu^0_{B-}$. Thus, we successfully determined the exact pressure dependence of α as $\alpha(P) = 0.0322P[\text{GPa}] + 0.601$. Moreover, the relationship of J to the pressure was also determined to be $J(P)/k_B[\text{K}] = -5.14[\text{K/GPa}]P[\text{GPa}] + 69.1$ [K]. Using these relations, the excitation energies observed at any pressure P were plotted against α in the form normalized by J. Figure 4a shows the result. A discontinuity in the excitation energy, which indicates a first-order transition, was again observed, and the critical ratio was determined to be $\alpha_{c1} = 0.660 \pm 0.003$.

The thick dotted lines in Fig. 4 are our calculated results, which agree very well with the obtained data. The results obtained using the 25T-CSM system [19] and those obtained using neutron inelastic scattering (INS) [35] agree well. The splitting, which is caused by the Dzyaloshinsky–Moriya (DM) interaction [39], observed in $v_{E\pm}^0$ is related to the high resolution of the setup. The result obtained by another theoretical calculation is also shown by the thin dashed-dotted line [42]. Although there is no splitting because the DM interaction is not taken into account, this calculation result is in good agreement with both the experimental data and our calculated results.

Theoretically, at the critical point α_{c1}(theory) ~ 0.68 [34, 42, 43], excitations change discontinuously as shown by the thick solid line, which was obtained by our calculation, thin solid and dotted lines [42]. Although the experimentally determined $\alpha_{c1} = 0.660$ is slightly smaller than α_{c1}(theory) ~ 0.68, the observed excitation energies were quantitatively consistent with these theoretical results. Therefore, we concluded that the observed transition is attributed to that from the dimer singlet state to the plaquette singlet state.

The neutron diffraction measurement under pressure has revealed the Néel order at 4.0 GPa [35]. By extending the pressure dependence of α obtained above, it was estimated that the critical ratio corresponding to this pressure was $\alpha_{c2} = 0.73$ (Fig. 4a). The recent theoretical calculation proposes that the phase boundary to the Néel phase is α_{c2}(theory) ~ 0.76 [34, 43]. Although it is slightly larger than the experimental result, a good agreement is also observed. The reason why the theoretically calculated phase boundaries to the plaquette phase and the Néel phase are larger than the experimental results is possibly owing to the interactions that have not been taken into account in the theory such as the exchange interaction between layers existing in the real system. Further quantitative research is expected in the future. Thus, the high-pressure THz ESR measurement revealed the phase transition from the dimer singlet state to the plaquette singlet state of this system.

4.2 Hemin: Model Case of Hemoproteins [44]

This is an application example of the 10T-CSM high-pressure ESR system. Metalloproteins are some of the essential proteins in the living body. A well-known example is hemoglobin, which transports oxygen. Its active center is heme (iron protoporphyrin IX) containing Fe^{2+} ion. The change in the coordination structure of the iron ion is essential for the unique ability to reversibly capture and release oxygen; thus, it is important to investigate the relationship between its structure and function. Pressure is a very useful parameter to control its structure. Hemin [iron (III) protoporphyrin IX chloride] is a model substance of heme and it is suitable as a stepping stone for future metalloprotein research by high-pressure THz ESR.

The structure of hemin includes four nitrogen atoms and one chlorine atom around Fe^{3+} ion ($S = 5/2$), as shown in the inset in Fig. 5a. This ligand field lifts the zero-field degeneracy of the three Kramers doublets of $S = 5/2$ of Fe^{3+} ion and provides the single ion magnetic anisotropy. The effect of ligand field is characterized by the zero-field splitting parameters D and E. Recently, the detailed values
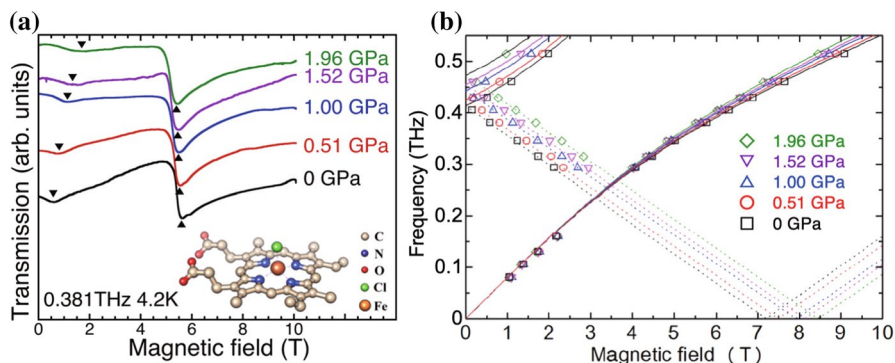
(a)

(b)

Fig. 5 **a** Pressure dependence of powder ESR spectra obtained at 0.381 THz and 4.2 K for hemin. **b** Frequency-field diagram at 4.2 K obtained at various pressures for hemin, made by modifying Fig. 4 in Ref. [44] (color online)

have been reported by the THz ESR measurements of hemin [45, 46]. As is shown later, the zero-field splitting of this system lies in the THz region and the THz ESR measurement is necessary to determine them directly.

Figure 5a is the pressure dependence of the ESR spectrum obtained for the powder sample, and Fig. 5b is its frequency-field diagram. As shown in these figures, hemin showed a large resonance field shift when pressure was applied. Because the intercept of the frequency axis provides the value of $2D$ directly, we can easily find that the D value increases with pressure. This result also indicates that the THz ESR measurement is very effective for its determination. The solid and dotted lines in the figure are the results of the simulation for the Hamiltonian of this system $\mathcal{H} = \mu_B \mathbf{S} \cdot \mathbf{g} \cdot \mathbf{H} + D S_z^2$, where μ_B is the Bohr magneton. It should be mentioned that the higher field and higher frequency are needed to observe the rhombic component E [45, 46]. From this simulation, it was determined that the D value changes from $+6.9$ to $+7.9$ cm^{-1} while the g_z value slightly decreases from 2.06 to 2.00. The former means that the easy plane anisotropy as the applied pressure is increased.

For hemin, a porphyrin ring is relatively rigid owing to its covalent bonds, and it is easily compressed perpendicular to the plane [44]. Therefore, the distance between iron and chlorine is considered to be more sensitive to pressure than that between iron and nitrogen atoms. Therefore, the application of pressure shortens the distance between iron and chlorine, which increases the energy of iron d_{yz} and d_{xz} orbitals. This enhances the easy plane anisotropy. Thus, high-pressure THz ESR is expected to be a powerful approach for sensitively detecting the change in electronic states of metalloproteins.

4.3 Hexagonal ABX$_3$-Type Antiferromagnet CsCuCl$_3$ [20]

This is an example of using the 15T-SM high-pressure ESR system. CsCuCl$_3$ (magnetic ion Cu^{2+}, $S = 1/2$) is a well-known substance, which shows a remarkable quantum effect [47]. There is a ferromagnetic chain along the c-axis and an antiferromagnet triangular lattice in the c-plane. The characteristic of this system is that the

ferromagnetic interaction is several times larger than the antiferromagnetic interaction, and there is a weak easy-plane type magnetic anisotropy[48]. The system has a 120° structure in the c-plane below the Néel temperature $T_N = 10.7$ K [49] and the magnetization shows a jump at $H_{c1} = 12.5$ T (1.1 K) when the magnetic field is applied parallel to the c-axis [50]. The theoretical study showed that this magnetization jump corresponds to the magnetic phase transition from the umbrella configuration stabilized by the easy-plane anisotropy to the coplanar configuration stabilized by quantum fluctuations [47]. In addition, a discontinuous change is seen in the AFMR mode at the corresponding field H_{c1} [51]. Figure 6a shows a frequency-field diagram obtained at 4.2K for $H \parallel c$ in this study. Indeed, the discontinuous change in the AFMR mode was confirmed at $H_{c1} = 10.9$ T as shown in Fig. 6a. Note here that modified field $H_m = (g/2)H$, where g is the g value in the paramagnetic state, was used in these figures. The g value was found not to depend on pressure, and it was obtained to be $g = 2.11$.

Recently, a so-called 1/3 magnetization plateau has been observed above the pressure of 0.68 GPa for $CsCuCl_3$ in its magnetization measurement under pressure [52]. The 1/3 magnetization plateau is a very typical quantum phenomenon expected in an ideal $S = 1/2$ triangular lattice antiferromagnet; however, few examples are known except for Cs_2CuBr_4 [53] and $Ba_3CoSb_2O_9$ [54]. Therefore, it has attracted considerable attention. In this study, we explored this material using high-pressure ESR.

Figure 6b is a frequency-field diagram at 4.2 K and 0.80 GPa for $H \parallel c$. There is the discontinuous change at $H_{c1} = 11.7$ T; in addition, a small change is observed at $H_{c2} = 13.1$ T. The region of $H_{c1} \leq H \leq H_{c2}$ was considered to correspond to the 1/3 plateau region from the comparison with the magnetization measurement under
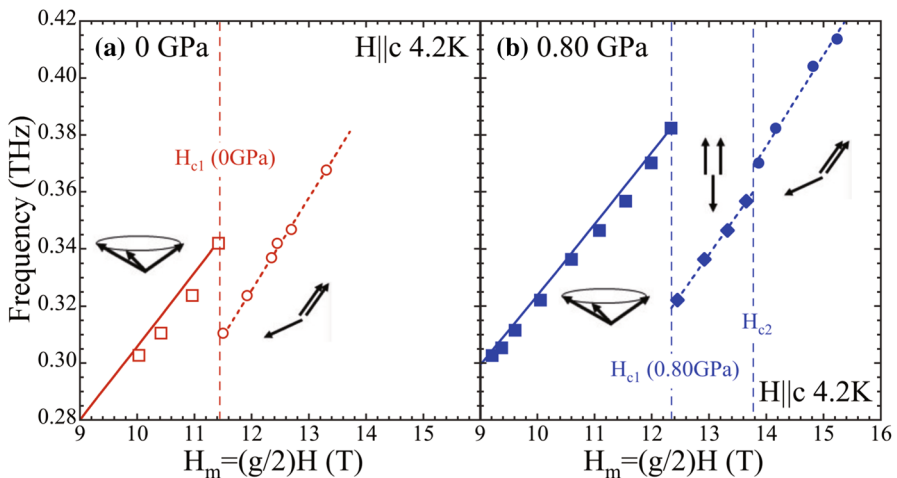

Fig. 6 Frequency-field diagram at 0 GPa (**a**) and 0.80 GPa (**b**) for $CsCuCl_3$ obtained at 4.2 K for $H \parallel c$. The horizontal axis is a modified field with $g = 2.11$. The solid lines are the fitting result of AFMR mode and the dotted lines are guides to the eye. **a** and **b** were made by modifying **a** and **b** in ref. [20], respectively (color online)

pressure. That is, at H_{c1}, the umbrella structure changes to the up–up–down structure, which is the magnetic structure corresponding to the 1/3 magnetization plateau; at H_{c2}, the up–up–down structure changes to the coplanar structure, as schematically shown in Fig. 6b. This is the first evidence of the 1/3 magnetization plateau from a microscopic point of view. We observed an increase in H_{c1} by applying pressure, and a similar tendency was observed in the magnetization measurement under pressure [52]. Moreover, the antiferromagnetic gap was observed to increase from 0.089 THz at 0 GPa to 0.119 THz at 0.80 GPa from the AFMR mode fitting [48], as shown in the solid lines in Fig. 6a and b. The investigation of origin of these increases in H_{c1} and an antiferromagnetic gap is on-going, and it is becoming clear that the relative increase in the antiferromagnetic interaction in the c plain to the intrachain ferromagnetic interaction is an important factor [55].

4.4 Anisotropic Triangular Lattice Antiferromagnet Cs$_2$CuCl$_4$ [56]

This is an application example of the 25T-CSM high-pressure ESR system. The triangular lattice antiferromagnet is a typical geometric frustration system. Specifically, when the spin quantum number is $S = 1/2$, it is expected that various quantum phases will appear owing to both quantum fluctuation and frustration effects [57]. If the distortion is introduced to the equilateral triangular lattice, or the magnitude of the quantum fluctuation is changed by applying magnetic field, further various phases are expected to appear [58, 59]. To confirm this, it is necessary to simultaneously control the exchange interaction and spin polarization; however, very few studies have been performed because such experiment is very difficult. Cs$_2$CuCl$_4$ (magnetic ion Cu^{2+}) has the spin quantum number of $S = 1/2$ and an anisotropic triangular lattice characterized by interactions J and J' (Fig. 7a, inset) [60]. Therefore, by applying the 25T-CSM high-pressure ESR system to this substance, this verification becomes possible.

Figure 7a shows the frequency-field diagram obtained under various pressures for this system, and Fig. 7b shows the typical pressure dependence of spectra for mode B obtained at 0.33 THz. They were obtained at 1.9 K which is above its Néel temperature $T_N = 0.62$ K [61]. Figure 7a shows that mode A is almost independent of pressure, whereas mode B is considerably depends on pressure. Mode B appears above the saturation magnetic field [62]. Although the system is in the paramagnetic state, it becomes the field-induced ferromagnetic state above the saturation field, and the magnetic structure effectively has a doubled period of the original lattice owing to the existence of the DM interaction [62]. Therefore, Brillouin zone folding occurs, which makes mode B observable; originally, it is a forbidden transition. The most characteristic feature is that the energy difference between modes A and B directly provides the interaction J' ($\hbar\Delta\omega = 4J'$). Moreover, in this study, we determined the saturation magnetic field from the resonant tunneling diode measurements under pressure. The saturation magnetic field is described by J and J'. These results shows that we successfully and accurately determined the relationship between pressure P and the interaction ratio J'/J. Furthermore, in the tunneling diode measurement below T_N under pressure, magnetic phase boundaries were observed, as shown
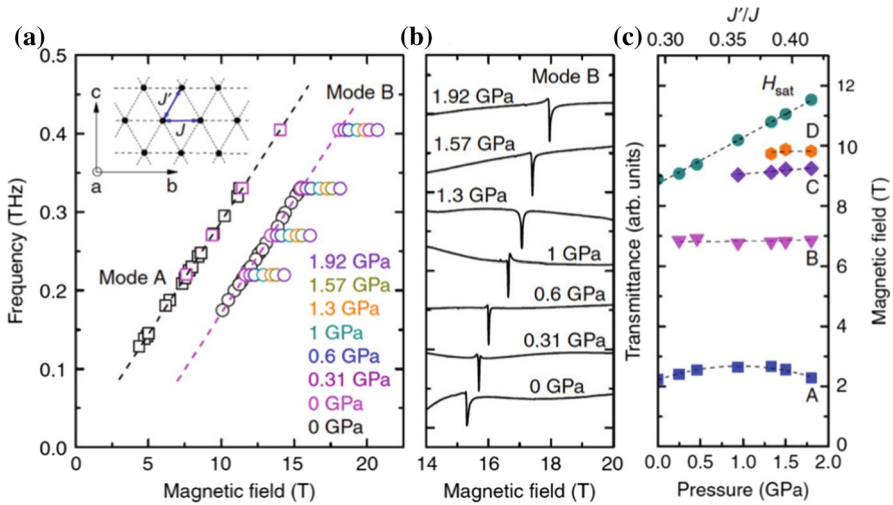
Fig. 7 a Frequency-field diagram for Cs_2CuCl_4 at 1.9 K obtained at various pressures for $H \parallel b$. **b** Pressure dependence of ESR spectra for mode B at 1.9 K for $H \parallel b$. **c** Field-pressure (J'/J) phase diagram obtained by the tunnel diode measurement at 350 mK for $H \parallel b$. **a**, **b** and **c** were reproduced from Fig. 1a, b and 3b in Ref. [56], respectively (color online)

in Fig. 7c, where new magnetic phases (represented by C and D) were discovered under high pressure and high magnetic field. It is expected that the phase diagram for the anisotropic triangular lattice for the interaction ratio J'/J (Fig. 7c) will stimulate further theoretical studies on quantum phase transitions in frustrated magnets.

5 Summary

High-pressure ESR was reviewed with a particular focus on measurements in the high-frequency region. Currently, there are three groups in the world that are capable of performing high-pressure high-frequency ESR measurements. Two groups, not including our group, performed high-sensitivity measurements at the expense of the frequency region. In contrast, our system can perform measurements at the high pressure of 2.5 GPa and in the wide frequency range of up to 0.8 THz, although the sensitivity is slightly lower than that of other groups. In our system, the use of ZrO_2-based ceramics for the internal parts of the pressure cell is essential because this material is tough and can transmit electromagnetic waves in the THz region. By showing several application examples, it is demonstrated that the high-pressure THz ESR measurement is very useful for investigating the pressure dependence of spin states of magnetic materials with energy structures in the sub-THz region. Specifically, the advantage that the pressure dependence of interaction parameters can be accurately determined is very significant because it allows us to compare experimental results with theoretical results.

Future studies may focus on further expanding pressure and magnetic field regions. Currently, we are developing new ceramics to improve toughness and/or

transmittance of electromagnetic waves. Although the use of pulsed high magnetic field without a reduction in both sensitivity and pressure region is extremely challenging, high-pressure THz ESR will be improved further if it becomes possible.

References

1. A. Avella, F. Mancini (eds.), *Strongly Correlated Systems Experimental Techniques (Springer*, Berlin, 2015), p. 173
2. K. Kawasaki, T. Sakurai, E. Ohmichi, S. Okubo, H. Ohta, K. Matsubayashi, Y. Uwatoko, Appl. Magn. Reson. **46**, 987 (2015)
3. C.P. Poole Jr., *Electron Spin Resonance* (Dover, New York, 1996), p. 337
4. S.K. Hoffmann, M. Krupski, W. Hilczer, Appl. Magn. Reosn. **5**, 407 (1993)
5. T. Sakurai, S. Okubo, H. Ohta, J. Magn. Reson. **280**, 3 (2017)
6. H. Ohta, S. Okubo, K. Kawakami, D. Fukuoka, Y. Inagaki, T. Kunimoto, Z. Hiroi, J. Phys. Soc. Jpn. **72**, 26 (2003)
7. H. Ohta, S. Okubo, T. Sakurai, T. Goto, K. Kirita, K. Ueda, Y. Uwatoko, T. Saito, M. Azuma, M. Takano, J. Akimitsu, Phys. B **294–295**, 624 (2001)
8. W.M. Walsh Jr., N. Bloembergan, Phys. Rev. **107**, 904 (1957)
9. N. Sakai, J.H. Pifer, Rev. Sci. Instr. **56**, 726 (1985)
10. A. Sienkiewicz, B. Vileno, S. Garaj, M. Jaworski, L. Forró, J. Magn. Reson. **177**, 261 (2005)
11. S.N. Lukin, P.V. Vodolazskiĭ, S.M. Ryabenko, Sov. J. Low Temp. Phys. **3**, 705 (1977)
12. A.Yu. Kozhukar', S.N. Lukin, G.A. Tsintsadze, V.A. Shapovalov, Cryogenics **16**, 441 (1976)
13. A.V. Kornilov, P.J.M. van Bentum, J.S. Brooks, J.S. Qualls, J.A.A.J. Perenboom, V.M. Pudalov, Synth. Met. **103**, 2246 (1999)
14. A.V. Kornilov, V.A. Sukhoparov, V.M. Pudalov, in *High Pressure Science and Technology*, ed. by W. Trzeciakowski (World Scientific, Singapore, 1996), p. 63
15. AB millimeter. http://www.abmillimetre.com/
16. T. Sakurai, A. Taketani, T. Tomita, S. Okubo, H. Ohta, Y. Uwatoko, Rev. Sci. Instr. **78**, 065107 (2007)
17. T. Sakruai, M. Tomoo, S. Okubo, H. Ohta, K. Kudo, Y. Koike, J. Phys. **150**, 042171 (2009)
18. T. Sakurai, K. Fujimoto, R. Matsui, K. Kawasaki, S. Okubo, H. Ohta, K. Matsubayashi, Y. Uwatoko, H. Tanaka, J. Magn. Reson. **259**, 108 (2015)
19. T. Sakurai, S. Kimura, M. Kimata, H. Nojiri, S. Awaji, S. Okubo, H. Ohta, Y. Uwatoko, K. Kudo, Y. Koike, J. Magn. Reosn. **296**, 1 (2018)
20. R. Okuto, E. Ohki, T. Sakurai, K. Hijii, H. Takahashi, E. Ohmichi, S. Okubo, H. Ohta, Y. Uwatoko, H. Tanaka, Appl. Magn. Reson. **50**, 1059 (2019)
21. B. Náfrádi, R. Gaál, A. Sienkiewicz, T. Fehér, L. Forró, J. Magn. Reson. **195**, 206 (2008)
22. B. Náfrádi, R. Gaál, T. Fehér, L. Forró, J. Magn. Reson. **192**, 265 (2008)
23. S. Hill. https://nationalmaglab.org/user-facilities/emr/emr-measurement-techniques/high-pressure-epr
24. A. Prescimone, C. Morien, D. Allan, J.A. Schlueter, S.W. Tozer, J.L. Manson, S. Parsons, E.K. Brechin, S. Hill, Angew. Chem. Int. Ed. **51**, 7490 (2012)
25. K. Thirunavukkuarasu, S.M. Winter, C.C. Beedle, A.E. Kovalev, R.T. Oakley, S. Hill, Phys. Rev. B **91**, 014412 (2015)
26. Á. Antal, T. Fehér, E.T. Szekeres, F. Fülöp, B. Náfrádi, L. Forró, A. Jánossy, Phys. Rev. B **84**, 075124 (2011)
27. H. Ohta, T. Sakurai, R. Matsui, K. Kawasaki, Y. Hirao, S. Okubo, K. Matsubayashi, Y. Uwatoko, K. Kudo, Y. Koike, J. Phys. Chem. B **119**, 13755 (2015)
28. T. Sakurai, R. Matsui, K. Kawasaki, S. Okubo, H. Ohta, K. Matsubayashi, Y. Uwatoko, K. Kudo, Y. Koike, Appl. Magn. Reson. **46**, 1007 (2015)

29. S. Awaji, K. Watanabe, H. Oguro, H. Miyazaki, S. Hanai, T. Tosaka, S. Ioka, Supercond. Sci. Technol. **30**, 065001 (2017)
30. T. Sakurai, Y. Hirao, K. Hijii, S. Okubo, H. Ohta, Y. Uwatoko, K. Kudo, Y. Koike, J. Phys. Soc. Jpn. **87**, 033701 (2018)
31. H. Kageyama, K. Yoshimura, R. Stern, N.V. Mushnikov, K. Onizuka, M. Kato, K. Kosuge, C.P. Slichter, T. Goto, Y. Ueda, Phys. Rev. Lett. **82**, 3168 (1999)
32. A. Koga, N. Kawakami, Phys. Rev. Lett. **84**, 4461 (2000)
33. S. Miyahara, K. Ueda, J. Phys. **15**, R327 (2003)
34. H. Nakano, T. Sakai, J. Phys. Soc. Jpn. **87**, 123702 (2018)
35. M.E. Zayed, Ch. Rüegg, J. Larrea, J.A.M. Läuchli, C. Panagopoulos, S.S. Saxena, M. Ellerby, D.F. McMorrow, Th Strässle, S. Klotz, G. Hamel, R.A. Sadykov, V. Pomjakushin, M. Boehm, M. Jiménez-Ruiz, A. Schneidewind, E. Pomjakushina, M. Stingaciu, K. Conder, H.M. Rønnow, Nat. Phys. **13**, 962 (2017)
36. T. Waki, K. Arai, M. Takigawa, Y. Saiga, Y. Uwatoko, H. Kageyama, Y. Ueda, J. Phys. Soc. Jpn. **76**, 073710 (2007)
37. S. Haravifard, A. Banerjee, J.C. Lang, G. Srajer, D.M. Silevitch, B.D. Gaulin, H.A. Dabkowska, T.F. Rosenbaum, Proc. Natl. Acad. Sci. USA **109**, 2286 (2012)
38. S. Haravifard, D. Graf, A.E. Feiguin, C.D. Batista, J.C. Lang, D.M. Silevitch, G. Srajer, B.D. Gaulin, H.A. Dabkowska, T.F. Rosenbaum, Nat. Commun. **7**, 11956 (2016)
39. O. Cépas, K. Kakurai, L.P. Regnault, T. Ziman, J.P. Boucher, N. Aso, M. Nishi, H. Kageyama, Y. Ueda, Phys. Rev. Lett. **87**, 167205 (2001)
40. H. Nojiri, H. Kageyama, K. Onizuka, Y. Ueda, M. Motokawa, J. Phys. Soc. Jpn. **68**, 2906 (1999)
41. H. Nojiri, H. Kageyama, Y. Ueda, M. Motokawa, J. Phys. Soc. Jpn. **72**, 3243 (2003)
42. Y. Takushima, A. Koga, N. Kawakami, J. Phys. Soc. Jpn. **70**, 1369 (2001)
43. P. Corboz, F. Mila, Phys. Rev. B **87**, 115144 (2013)
44. T. Okamoto, E. Ohmichi, Y. Saito, T. Sakurai, H. Ohta, J. Phys. Chem. B **122**, 6880 (2018)
45. J. Nehrkorn, B.M. Martins, K. Holldack, S. Stoll, H. Dobbek, R. Bittl, A.M. Schnegg, Physics **111**, 2696 (2013)
46. T. Okamoto, E. Ohmichi, S. Okubo, H. Ohta, J. Phys. Soc. Jpn. **87**, 013702 (2018)
47. T. Nikuni, H. Shiba, J. Phys. Soc. Jpn. **62**, 3268 (1993)
48. H. Tanaka, U. Schotte, K.D. Schotte, J. Phys. Soc. Jpn. **61**, 1344 (1992)
49. K. Adachi, N. Achiwa, M. Mekata, J. Phys. Soc. Jpn. **49**, 545 (1980)
50. H. Nojiri, Y. Tokunaga, M. Motokawa, J. Phys. **49**(C8), 1459 (1988)
51. H. Ohta, S. Imagawa, M. Motokawa, H. Tanaka, J. Phys. Soc. Jpn. **62**, 3011 (1993)
52. A. Sera, Y. Kousaka, J. Akimitsu, M. Sera, K. Inoue, Phys. Rev. B **96**, 014419 (2017)
53. T. Ono, H. Tanaka, H.A. Katori, F. Ishikawa, H. Mitamura, T. Goto, Phys. Rev. B **67**, 104431 (2003)
54. T. Susuki, N. Kurita, T. Tanaka, H. Nojiri, A. Matsuo, K. Kindo, H. Tanaka, Phys. Rev. Lett. **110**, 267201 (2013)
55. D. Yamamoto, T. Sakurai, R. Okuto, S. Okubo, H. Ohta, in *Proceedings of the 75th Annual Meeting of Physical Society of Japan* (Nagoya, Japan, 16–19 March 2020) p. 1101
56. S.A. Zvyagin, D. Graf, T. Sakurai, S. Kimura, H. Nojiri, J. Wosnitza, H. Ohta, T. Ono, H. Tanaka, Nat. Commun. **10**, 1064 (2019)
57. D. Yamamoto, G. Marmorini, I. Danshita, Phys. Rev. Lett. **112**, 127203 (2014)
58. O.A. Starykh, H. Katsura, L. Balents, Phys. Rev. B **82**, 014421 (2010)
59. O.A. Starykh, W. Jin, A.V. Chubukov, Phys. Rev. Lett. **113**, 087204 (2014)
60. R. Coldea, D.A. Tennant, A.M. Tsvelik, Z. Tylczynski, Phys. Rev. Lett. **86**, 1335 (2001)
61. R. Coldea, D.A. Tennant, R.A. Cowley, D.F. McMorrow, B. Dorner, Z. Tylczynski, J. Phys. **8**, 7473 (1996)
62. S.A. Zvyagin, D. Kamenskyi, M. Ozerov, J. Wosnitza, M. Ikeda, T. Fujita, M. Hagiwara, A.I. Smirnov, T.A. Soldatov, A.Ya. Shapiro, J. Krzystek, R. Hu, H. Ryu, C. Petrovic, M.E. Zhitomirsky, Phys. Rev. Lett. **112**, 077206 (2014)